

1 Polarization Switching and Light-Enhanced Piezoelectricity in Lead 2 Halide Perovskites

3 Mariona Coll,^{*,†} Andrés Gomez,[†] Elena Mas-Marza,[‡] Osbel Almora,[‡] Germà Garcia-Belmonte,[‡]
4 Mariano Campoy-Quiles,[†] and Juan Bisquert^{*,‡,§}

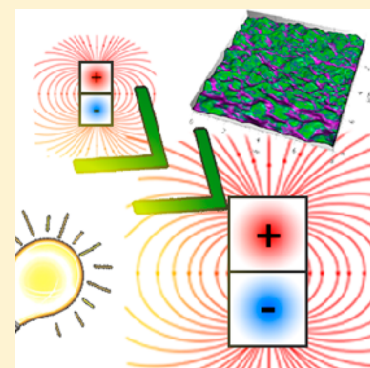
5 [†]Institut de Ciència de Materials de Barcelona (ICMAB-CSIC), Campus UAB, 08193, Bellaterra, Catalonia, Spain

6 [‡]Photovoltaics and Optoelectronic Devices Group, Departament de Física, Universitat Jaume I, 12071, Castelló, Spain

7 [§]Department of Chemistry, Faculty of Science, King Abdulaziz University, Jeddah 22254, Saudi Arabia

8 **S** Supporting Information

9 **ABSTRACT:** We investigate the ferroelectric properties of photovoltaic methylammo-
10 nium lead halide $\text{CH}_3\text{NH}_3\text{PbI}_3$ perovskite using piezoelectric force microscopy (PFM) and
11 macroscopic polarization methods. The electric polarization is clearly observed by
12 amplitude and phase hysteresis loops. However, the polarization loop decreases as the
13 frequency is lowered, persisting for a short time only, in the one second regime, indicating
14 that $\text{CH}_3\text{NH}_3\text{PbI}_3$ does not exhibit permanent polarization at room temperature. This
15 result is confirmed by macroscopic polarization measurement based on a standard
16 capacitive method. We have observed a strong increase of piezoelectric response under
17 illumination, consistent with the previously reported giant photoinduced dielectric
18 constant at low frequencies. We speculate that an intrinsic charge transfer photoinduced
19 dipole in the perovskite cage may lie at the origin of this effect.



20 **V**ery high power conversion efficiencies of sunlight to
21 electricity have been obtained for photovoltaic devices
22 based on hybrid inorganic–organic lead halide perovskites in a
23 short time of research.^{1–4} Methylammonium lead halide
24 materials as $\text{CH}_3\text{NH}_3\text{PbI}_3$ (MAPbI₃) and the associated
25 substitutional variants display excellent photovoltaic properties
26 in terms of light absorption, electronic charge separation,
27 transport and recombination. These materials provide a very
28 promising novel route to massive solution-based facile
29 fabrication of low cost solar cells. However, the chemical and
30 structural properties of the inorganic–organic perovskite, which
31 are unprecedented in the previously known high efficiency
32 photovoltaic materials, produce a number of physical features
33 that are not understood and are intensely investigated at
34 present. In the hybrid perovskite structure ABX_3 , the organic
35 cation A^+ is in a cage formed by four BX_6 octahedra. It has
36 become evident that under photovoltaic operation (light or
37 voltage biasing), the “soft” structure of the hybrid perovskite,
38 associated with the combination of organic and inorganic ionic
39 components, produces peculiar and significant phenomena in
40 the ultraslow time regime as current–voltage hysteresis^{5,6} and
41 persistent photovoltage decay.^{7–9} These properties have been
42 assigned to either ferroelectric or ionic polarization, or else to
43 electronic traps.^{10,11} Another connection between structure and
44 electronic response is established by the giant dielectric
45 constant observed in MAPbI₃, that is strongly enhanced by
46 illumination. This property has been observed by capacitance
47 spectroscopy¹² and suggests the formation of a large photo-
48 induced dipole.¹³

49 This paper investigates the ferroelectric polarization that may
50 have a substantial impact on device operation and give rise to
51 novel applications of the inorganic–organic lead halide
52 perovskites in multiferroic materials.¹⁴ In general, many oxide
53 perovskites are highly polar and show a ferroelectric response
54 that provides a static dielectric constant in the order of 10^3 .
55 MAPbI₃ with tetragonal symmetry belongs to the $4mm$ point
56 group and $I4/mcm$ space group and as such could be
57 ferroelectric. The polarization P in hybrid perovskites may
58 arise from three major mechanisms: the ionic off-centering, the
59 atomic BX_6 cage rotations, and the rotation of dipolar MA^+ .
60 The latter mechanism is facile,¹⁵ and it has been favored in
61 recent simulation studies of polarization in MAPbI₃,^{16–18} as
62 dipole rotation is simpler to treat than cooperative ionic
63 displacements. Former studies,^{19,20} both for $\text{CH}_3\text{NH}_3\text{PbI}_3$ and
64 $\text{CH}_3\text{NH}_3\text{PbBr}_3$, showed that at room temperature, the PbX_6
65 octahedra rotate alternatively around the c -axis conforming the
66 SrTiO_3 -type tetragonal perovskite structure, and the rotation
67 angle of the PbI_6 octahedra increases with decreasing
68 temperature. The transition from tetragonal to orthorhombic
69 phase is accompanied by a peak of the dielectric constant,
70 suggesting that the orthorhombic phase is ferroelectric. More
71 recently, the local dipole structure property has been invoked to
72 explain a giant dielectric constant,¹² slow dynamic response¹⁰
73 and current–voltage hysteresis.^{21,22} However, local polarization

Received: March 10, 2015

Accepted: March 30, 2015

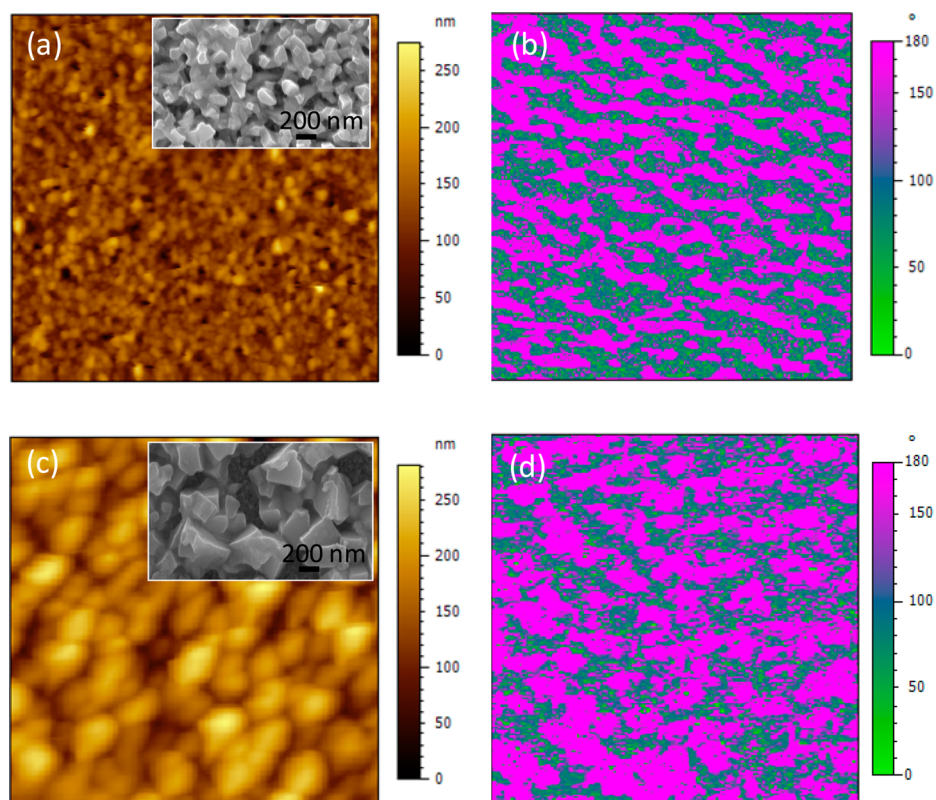


Figure 1. PFM analysis of MAPbI₃ films. (a) Topographic and (b) out-of-plane PFM-phase image of MAPbI₃ films with small crystals. (c) Topographic and (d) out-of-plane PFM phase image of MAPbI₃ films with large crystals. Image size is 8 μm × 8 μm. PFM phase image is in false color. The insets show SEM images of the corresponding samples.

74 distortion may be combined with long-range ionic drift that
75 establishes macroscopic polarization at the contacts of the
76 sample.⁶

77 Importantly, there are only a few direct observations of
78 polarization features of inorganic–organic lead halide perov-
79 skites, and the results reported so far are not conclusive. One
80 study²³ claimed the direct observation of ferroelectric domains,
81 while another one reported the absence of such effects.¹¹
82 Piezoelectric force microscopy (PFM) is a variant of AFM that
83 is widely used to image polarization structure and local
84 switching. However, the observation of contrast region is not
85 sufficient evidence for the existence of ferroic domains, since
86 such contrast may be due to several factors, namely: the
87 existence of ferroelectric domains, electrochemical phenomena,
88 ion migration, electrostatic effects, and it can also have a
89 contribution from surface topography.^{24–26} Nevertheless, the
90 states of opposite polarization under applied bias are clearly
91 revealed by a *change of phase* of ac voltage, since the
92 piezoelectric response has different sign in either state of
93 polarization, and this method is shown below. Another
94 important point is whether voltage induced polarization
95 remains permanent, as in ferroelectric material, or disappears
96 when the external voltage is removed.

97 In order to obtain a clear picture of polarization in MAPbI₃,
98 we have investigated polarization switching, the light depend-
99 ence and the relaxation time in MAPbI₃, using PFM and
100 macroscopic polarization measurement. The structure of the
101 samples prepared as indicated in Experimental methods
102 consists of FTO/TiO₂ buffer layer/TiO₂ mesoporous layer
103 (200 nm)/MAPbI₃. The samples were measured without upper
104 contact, but their related solar cells provided a power

conversion efficiency of about 9% with a photovoltage of ca. 105
1 V (see SI). Samples with different crystal size have been 106
prepared²⁷ with the aim to investigate a possible interaction 107
between morphology and polarizability. Topographic images 108
were acquired simultaneously with the PFM-phase images. 109
From the topographic image, the samples with small MAPbI₃ 110
crystals display a surface roughness (rms) of 25 nm and an 111
average crystal size diameter of 200 nm (Figure 1a), whereas 112
samples with large MAPbI₃ crystals show a rms of 38 nm and a 113
measured crystal size diameter of 500 nm (Figure 1c). This 114
morphological analysis is in good agreement with the scanning 115
electron microscopy (SEM) study as shown in the correspond- 116
ing inset images. 117

High humidity conditions (80–90%) can promote the 118
existence of electrochemical phenomena between the tip and 119
the sample surface, which can lead to surface damage and 120
misinterpretation of PFM data.²⁸ In order to minimize the 121
amount of water layers between the tip and the sample surface 122
and therefore minimize the existence of electrochemical 123
reactions, we performed the experiments under low humidity 124
conditions (<5%). Importantly, careful inspection of the surface 125
topography before and after the acquisition of the PFM image 126
indicates that no undesired topography changes occurred 127
during the PFM measurement. 128

The PFM-phase images of both samples show a significant 129
phase contrast (see Figure 1b,d). Interestingly, no correlation 130
between the domain shape and location and surface grain 131
morphology was observed (see Figure 1a,c). This suggests a 132
minimal contribution from the surface topography on the PFM- 133
phase contrast image. Qualitative analysis of the two colored 134
areas (false colors), showed that the pink areas results in 38% ± 135

136 5 for the small crystal samples and $45\% \pm 5$ for the large crystal
 137 samples, Figure 1b and d respectively, which rule out any
 138 crystal size dependence. Previous PFM studies on solution-
 139 processed MAPbI₃ thin films attributed similar piezo-phase
 140 contrast to ferroelectric domains.²³ However, it is not
 141 straightforward from the PFM phase image to discriminate
 142 between charge accumulation and ferroelectric domains;²⁴
 143 therefore, extra characterization is required. In-field hysteresis
 144 loops using a 140 V/s scan rate were obtained by measuring the
 145 piezoresponse in the presence of an electric field. Representa-
 146 tive locally measured PFM-amplitude and phase loops for both
 147 samples are shown in Figure 2. The observed 180° phase switch

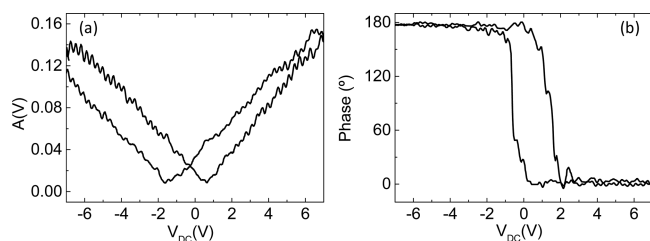


Figure 2. (a) Piezo amplitude and (b) Piezo-phase hysteresis loops of MAPbI₃ thin films recorded at a 140 V/s scan rate.

148 indicates a switchable portion of spontaneous polarization.²⁹
 149 These results are in contrast to the work published by Xiao et
 150 al. where they obtained a flat signal when measuring both the
 151 PFM hysteresis loops and the macroscopic ferroelectric
 152 polarization loops, using a 0.08 V/s scan rate.¹¹ One major
 153 difference between the two measurements is the scan rates,
 154 which might suggest that these halide perovskites present a
 155 poor (if any) polarization retention, as we demonstrate below.
 156 Remanent loops (measurement in the absence of DC field)
 157 further confirmed the lack of ferroelectric retention in MAPbI
 158 films.

159 We performed a series of piezo-phase loops in a range of
 160 0.1–10 s acquisition times (corresponding to 140–1.4 V/s scan
 161 rates) and analyzed the evolution of the coercivity (see Figure
 162 3a,b). It is clearly observed that the coercivity decays with time

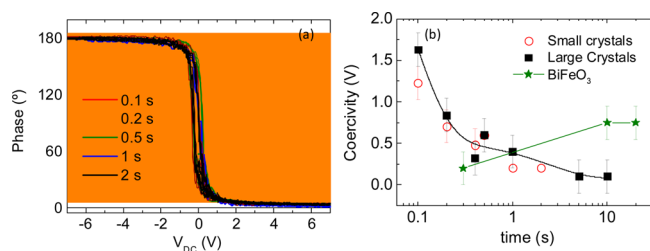


Figure 3. (a) Piezo-phase hysteresis loops of MAPbI₃ thin films with small crystals performed at different acquisition times. (b) Coercivity dependence with time of MAPbI₃ films with small (red open circles) and large crystals (black squares) and 25 nm BiFeO₃ thin films (green stars).

163 and beyond 1s decreases by a factor of 2. By contrast, the
 164 coercivity evolution of a typical ferroelectric perovskite oxide
 165 such as BiFeO₃ film, increases from 0.3 to 10 s, being retained
 166 for several hours and even months.³⁰ No significant difference
 167 in the retention behavior is identified when comparing MAPbI₃
 168 samples with small and big crystals, Figure 3b. We next carried
 169 out the experiment to electrically write (pole) with the AFM
 170 probe an area of $4 \mu\text{m} \times 4 \mu\text{m}$ with -7 V DC bias and then

pole back an inner area of $2 \mu\text{m} \times \mu\text{m}$ with $+7 \text{ DC}$. When
 171 imaging this area, and contrary to the case of well-known
 172 ferroelectric materials such as BiFeO₃, there is no visible change
 173 in the PFM-phase image (see Supporting Information Figure
 174 S3). Note that the whole process (writing and reading) takes 8
 175 min to complete, which is much larger than the time scales of
 176 the coercivity decay obtained above (Figure 3b). From these
 177 data we can confirm that polarization retention in these
 178 MAPbI₃ films occurs only for very short times. 179

In order to further corroborate the absence of ferroelectric
 180 retention in MAPbI₃ films, macroscopic polarization P analyses
 181 with respect to electrical field E were carried out using the
 182 classical Sawyer–Tower circuit (inset of Figure 4). This 183 #

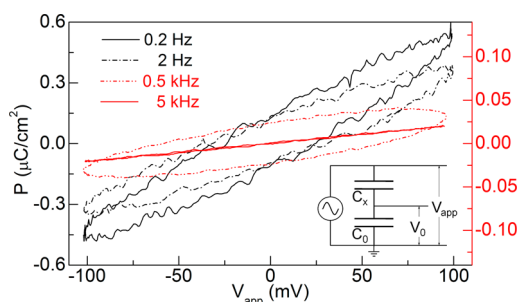


Figure 4. Polarization tests of large crystal MAPbI₃-based complete solar cells using the Sawyer–Tower circuit in the inset. At high frequencies, the response is purely capacitive. At low frequencies, elliptic traces indicate the angular phase shift produced by resistive elements.

184 experiment allows recording hysteresis P – E loops by polarizing
 185 the sample and registering the induced charge in the plates of a
 186 reference capacitor. We used the testing circuit to explore the
 187 existence of ferroelectric hysteresis loops with large crystal
 188 MAPbI₃-based complete solar cells using *spiro*-OMeTAD/Au
 189 top contacts. When high-frequencies are used in the polarizing
 190 voltage source (5 kHz) only purely capacitive responses are
 191 obtained as observed in Figure 4b. Since piezo-phase loops in
 192 Figure 3a show coercivity decay in the range of seconds, low-
 193 frequency P – E loops were also checked. As shown in Figure 4,
 194 only linear responses (ellipses) are obtained. These loops occur
 195 as a consequence of the series connection of resistive and
 196 capacitive elements. Importantly, the resistance introduces a
 197 time delay that tends to disappear as the perturbation frequency
 198 is reduced. In agreement with our previous PFM analysis,
 199 ferroelectric features were not found by macroscopic polar-
 200 ization tests in MAPbI₃ films.

In another set of experiments, we investigated the PFM
 201 response of MAPbI₃ films under illumination with white light
 202 from a LED with 4.5 mW power (PFM setup shown in the
 203 Supporting Information, Figure S5). Under such conditions, we
 204 observed no change in the piezo-phase hysteresis loops, nor in
 205 the retention times. 206

The effective piezoelectric coefficient of the MAPbI₃ films,
 207 d_{zz} , was derived from the linear dependence between an
 208 averaged tip oscillation amplitude A according to $A = d_{zz} V_{AC}$ ³¹
 209 obtaining 5 pm/V and 6 pm/V for the small and large crystal
 210 samples, respectively (see Supporting Information Figure S2).
 211 To the best of our knowledge, there are no examples in the
 212 literature regarding theoretical values of the piezoelectric
 213 coefficient of perovskite halides. As a reference, values between 214

215 10 and 50 pm/V are typically reported for 0.2–0.6 μm nm lead
 216 zirconate titanate (PZT) ferroelectric films.³²
 217 Interestingly, we also measured the effective piezoelectric
 218 coefficient under white light and found that it dramatically
 219 increased up to 25 pm/V (see Figure 5a). Note that the

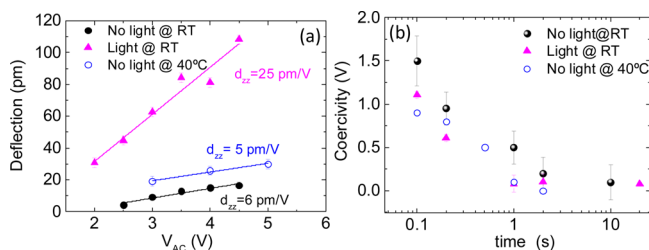


Figure 5. (a) Deflection versus V_{AC} and (b) coercivity dependence with time for MAPbI₃ films in the dark at room temperature (RT) (black circles), under illumination (pink triangles) and in dark and at 40 °C (blue open circles).

220 observed increase in the d_{zz} coefficient under illumination is in
 221 sharp contrast with the results of previous studies^{33,34}
 222 performed on ferroelectric PZT films, where it was observed
 223 that the UV light (under weak electric field) induced a decrease
 224 in the piezoelectric coefficient explained by a reduction of the
 225 overall polarization. The magnitude of the bulk polarization of
 226 MAPbI₃ has been predicted to be 38 $\mu\text{C}/\text{cm}^2$ based on the
 227 molecular dipole moment 2.29D of the cation MA⁺.^{16,35}
 228 However, the dielectric constant increases strongly at low
 229 frequencies, and furthermore a photoinduced giant dielectric
 230 constant has been observed in MAPbI₃ films.¹² An internal
 231 charge transfer transition upon light excitation may lead to a
 232 large added dipole moment. By means of modulation
 233 electroabsorption (EA) spectroscopy, Wu et al.¹³ calculated a
 234 change of the electronic dipole moment, $\Delta\mu$, (from ground
 235 state to excited state) of 288 D, which is notably larger than the
 236 change observed in other widely studied photosensitive
 237 materials such as CdSe ($\Delta\mu \sim 20\text{--}30$ D). Therefore, the
 238 impressive increase in the d_{zz} coefficient identified by PFM
 239 under illumination (Figure 5a) can also be related to the
 240 formation of large photoinduced dipole moments, in agreement
 241 with previous observations by different experimental techni-
 242 ques.

243 We would like to note again that when measuring the
 244 coercivity under illumination with different scanning rates, no
 245 differences were observed from the measurements performed in
 246 dark (see Figure 5b). Therefore, although the piezoelectric
 247 coefficient is 4 times larger, the kinetics under illumination
 248 follows the same trend as in dark, i.e., small retention (< 2s).

249 PFM measurements were also performed on a photosensitive
 250 organic material, namely, region regular poly(3-hexyl thio-
 251 phene) blended with fullerene soluble derivative (PCBM),
 252 where no piezoelectric/ferroelectric behavior is expected.
 253 Reassuringly, we did not observe PFM domains, nor the
 254 typical phase and amplitude loops (see Supporting Information,
 255 Figure S4e,g). Consequently, by comparing the PFM behaviors
 256 obtained for these two photovoltaic materials, we suggest that
 257 the PFM response exhibited by MAPbI₃ films is unlikely due to
 258 charge accumulation effects arising from photogenerated
 259 charges.

260 Finally, we have also investigated the influence of temper-
 261 ature (RT, 40 °C, 60 °C) on the polarization in order to rule
 262 out any temperature-dominated phenomena in the piezores-

263 ponsion signal. No changes in the domain features were identified
 264 in the PFM phase image when exposed to temperatures up to
 265 50 °C (see Supporting Information Figure S6). Considering
 266 that no phase transition would be expected at temperatures <60
 267 °C,³⁶ the coercivity evolution with time and piezoelectric
 268 coefficient were evaluated at 40 °C (see Figure 5). The film
 269 behaves in the same way at 40 °C as at room temperature in
 270 terms of domain sizes, coercivity, and retention times. This fact
 271 rules out temperature-related artifacts on the light-induced
 272 piezoelectric coefficient increase demonstrated above.

273 In summary, MAPbI₃ films with a TiO₂ contact have been
 274 investigated by PFM. The films show large polarizability.
 275 Polarization is confirmed by piezo-phase loops that are
 276 reported here for the first time. However, at room temperature,
 277 MAPbI₃ in tetragonal phase has poor polarization retention and
 278 it is not ferroelectric. In fact, the coercivity decays in the time
 279 regime of seconds, which is in agreement with the recent
 280 interpretation of structural relaxation in photovoltage decays.⁸
 281 In addition, we have observed a strong increase of the
 282 piezoelectricity when carriers are photogenerated in the
 283 MAPbI₃ film, which correlates to a previous observation of a
 284 photoinduced giant dielectric constant. This observation points
 285 to an intrinsic nature of voltage induced polarization in MAPbI₃
 286 film, in the sense that the polarization is local and caused by
 287 rotation of dipoles or other structural units, with the formation
 288 of polarized domains with relatively slow depolarization times.
 289 Such local units, so far unidentified, may be strongly enhanced
 290 in the presence of photogenerated carriers. However, ion
 291 motion still forms a source of “extrinsic” polarization, located at
 292 contacts and dependent on sample configuration, and both
 293 types of polarization effect may take place depending on sample
 294 type.

295 ■ EXPERIMENTAL METHODS

296 Solvents and reagents are commercially available and were used
 297 as received from commercial suppliers. CH₃NH₃I was
 298 synthesized by the reaction of 0.273 mol of a solution of
 299 CH₃NH₂ in ethanol with 0.223 mol of aqueous HI, at 0 °C for
 300 4 h. Then, the volatile compounds were removed under
 301 reduced pressure; the resulting CH₃NH₃I was recrystallized
 302 from ethanol/diethyl ether and dried under vacuum overnight.

303 *CH₃NH₃PbI₃ (MAPbI₃) Perovskite Films Preparation.* Fluorine-
 304 doped tin oxide (FTO) coated glass sheets (2.5 × 2.5 mm,
 305 Pilkington TEC15, ~ 15 Ω/sq resistance) were cleaned with
 306 soap (Hellmanex) and rinsed with Milli-Q water and ethanol.
 307 Then, the sheets were sonicated for 15 min in a solution of
 308 acetone:isopropanol (1:1 v/v), rinsed with ethanol, and dried
 309 with compressed air. After that, a UV/ozone treatment was
 310 performed for 15 min. Then, a compact TiO₂ blocking layer
 311 was deposited onto the substrates by spray pyrolysis at 450 °C,
 312 using a titanium diisopropoxide bis(acetylacetonate) (75% in
 313 isopropanol, Sigma-Aldrich) solution diluted in ethanol (1:39,
 314 v/v), with oxygen as carrier gas. Then, the films were kept at
 315 450 °C for 5 min. A UV/ozone treatment was performed for 15
 316 min. On top of the compact layer, a 200 nm-thick mesoporous
 317 TiO₂ layer was deposited by spin coating at 4000 rpm for 30 s
 318 using a TiO₂ paste (Dyesol 18NRT, 20 nm average particle
 319 size) diluted in terpineol (1:3, weight ratio). After drying at 80
 320 °C for 10 min, the TiO₂ layers were annealed at 470 °C for 30
 321 min and cooled to room temperature. The mesoporous layer
 322 was further treated with 20 mM of aqueous TiCl₄·(THF)₂
 323 solution at 70 °C for 10 min, and annealed at 500 °C during 30
 324 min. After a UV/ozone treatment for 15 min, 30 μL of a 1.082

325 M solution of PbI_2 in dimethylformamide was spin-coated onto
 326 the mesoporous layer at 500 rpm for 5 s and 6000 rpm for 20 s,
 327 followed by heating at 40 °C for 3 min and 100 °C for 10 min
 328 on a hot plate. The PbI_2 film was then dipped for 1 min in a
 329 solution of $\text{CH}_3\text{NH}_3\text{I}$ in isopropanol (0.044 M for large crystal
 330 size and 0.063 M for small crystal size), spun at 500 rpm for 5 s,
 331 1500 rpm for 10 s, and 3000 rpm for 20 s, and heated at 40 °C
 332 for 3 min and at 100 °C for 10 min on a hot plate.

333 BiFeO_3 was grown by atomic layer deposition at 250 °C and
 334 post annealed at 650 °C (unpublished results). Regioregular
 335 poly(3-hexylthiophene) and PCBM were purchased from
 336 Sigma-Aldrich and used as received. Films were prepared by
 337 knife coating a 30 mg/mL solution in chlorobenzene on top of
 338 a 40 nm thick PEDOT:PSS-coated ITO glass substrate.

339 *Piezoelectric Force Microscopy (PFM) Measurement.* PFM
 340 measurements were performed with an Agilent 5500LS
 341 instrument using a rmn-25pt300 tip with a spring constant of
 342 18 N/m. Measurement conditions were kept in a ambient
 343 humidity below 5%. PFM measurements were performed in
 344 dark and under illumination (4.5 mW). The AC frequency was
 345 set to ≈ 122 kHz, and its amplitude to 0.5 V. The cantilever
 346 deformation has been calibrated using a force–distance curve.
 347 The effective piezoelectric coefficient of the MAPI film, d_{zz} , was
 348 derived from the linear dependence between an averaged tip
 349 oscillation amplitude A according to $A = d_{zz}V_{AC}$.

350 *PFM under Illumination.* To perform these measurements, we
 351 have designed a PFM sample holder made of copper where we
 352 can shine light from the bottom using a LED integrated within
 353 the holder (see Figure S5). Sample temperature under
 354 illumination was measured using a PT1000 sensor at three
 355 different sample locations being the typical values all around 22
 356 °C.

357 *PFM at 40–60 °C.* The heating was performed using a
 358 constant current source connected to a ceramic heater. To
 359 measure the temperature, we used a PT1000 sensor located at 1
 360 mm apart from the sample's backside. After acquiring the
 361 images, the topside temperature of the sample was measured
 362 using another PT1000 sensor to ensure a correct assignment of
 363 the surface's temperature, and a 13° difference was found.
 364 Temperatures described in the manuscript are already the
 365 surface temperature. Macroscopic polarization loops were
 366 investigated by means of the classical Sawyer–Tower circuit
 367 (inset Figure 4) in which a voltage source polarizes the series
 368 connection of the investigated sample and a reference capacitor
 369 C_0 . The charge induced in the sample was monitored by means
 370 of the potential drop at the capacitor as $P = C_0V_0$. For high
 371 enough reference capacitor values, the bias voltage mainly
 372 drops at the sample.

373 *Structural Characterization.* The morphology and structural
 374 properties of the films were analyzed using a JEOL 7001F
 375 scanning electron microscope with a film emission gun
 376 (SEM-FEG). Phase purity and film crystallinity were studied
 377 by using a GADDS X-ray diffractometer equipped with a 2D X-
 378 ray detector with $\text{Cu-K}\alpha$ $\lambda = 1.5418$ Å (see Supporting
 379 Information Figure S1).

380 ■ ASSOCIATED CONTENT

381 ● Supporting Information

382 Additional figures and details as described in the text. This
 383 material is available free of charge via the Internet [http://pubs.](http://pubs.acs.org)
 384 [acs.org](http://pubs.acs.org).

385 ■ AUTHOR INFORMATION

386 Corresponding Authors

*E-mail: mcoll@icmab.es (M.C.) 387

*E-mail: jbisquert@uji.es (J.B.). 388

389 Notes

The authors declare no competing financial interest. 390

391 ■ ACKNOWLEDGMENTS

We acknowledge financial support from the Spanish Ministerio 392
 de Economía y Competitividad (MINECO) through RyC 393
 contracts 2013-12448 and 2011-07726 and projects MAT2013- 394
 47192-C3-1-R and MAT2012-37776. We thank Sang-Woo Kim 395
 and Ignasi Fina for fruitful discussions. 396

397 ■ REFERENCES

- (1) Kojima, A.; Teshima, K.; Shirai, Y.; Miyasaka, T. *Organometal Halide Perovskites as Visible-Light Sensitizers for Photovoltaic Cells.* *J. Am. Chem. Soc.* **2009**, *131*, 6050–6051. 398
- (2) Kim, H.-S.; Lee, C.-R.; Im, J.-H.; Lee, K.-B.; Moehl, T.; Marchioro, A.; Moon, S.-J.; Humphry-Baker, R.; Yum, J.-H.; Moser, J. E.; et al. Lead Iodide Perovskite Sensitized all-Solid-State Submicron Thin Film Mesoscopic Solar Cell with Efficiency Exceeding 9%. *Sci. Rep.* **2012**, *2*, 591. 399
- (3) Lee, M. M.; Teuscher, J.; Miyasaka, T.; Murakami, T. N.; Snaith, H. J. Efficient Hybrid Solar Cells Based on Meso-Superstructured Organometal Halide Perovskites. *Science* **2012**, *338*, 643–647. 400
- (4) Jeon, N. J.; Noh, J. H.; Yang, W. S.; Kim, Y. C.; Ryu, S.; Seo, J.; Seok, S. I. Compositional Engineering of Perovskite Materials for High-Performance Solar Cells. *Nature* **2015**, *517*, 476–480. 401
- (5) Snaith, H. J.; Abate, A.; Ball, J. M.; Eperon, G. E.; Leijtens, T.; Noel, N. K.; Stranks, S. D.; Wang, J. T.-W.; Wojciechowski, K.; Zhang, W. Anomalous Hysteresis in Perovskite Solar Cells. *J. Phys. Chem. Lett.* **2014**, *5*, 1511–1515. 402
- (6) Unger, E. L.; Hoke, E. T.; Bailie, C. D.; Nguyen, W. H.; Bowring, A. R.; Heumüller, T.; Christoforo, M. G.; McGehee, M. D. Hysteresis and Transient Behavior in Current-Voltage Measurements of Hybrid-Perovskite Absorber Solar Cells. *Energy Environ. Sci.* **2014**, *7*, 3690–3698. 403
- (7) Baumann, A.; Tvingstedt, K.; Heiber, M. C.; Vath, S.; Momblona, C.; Bolink, H. J.; Dyakonov, V. Persistent Photovoltage in Methylammonium Lead Iodide Perovskite Solar Cells. *APL Mater.* **2014**, *2*, 081501. 404
- (8) Bertoluzzi, L.; Sanchez, R. S.; Liu, L.; Lee, J.-W.; Mas-Marza, E.; Han, H.; Park, N.-G.; Mora-Sero, I.; Bisquert, J. Cooperative Kinetics of Depolarization in $\text{CH}_3\text{NH}_3\text{PbI}_3$ Perovskite Solar Cells. *Energy Environ. Sci.* **2015**, *8*, 910–915. 405
- (9) Pockett, A.; Eperon, G. E.; Peltola, T.; Snaith, H. J.; Walker, A. B.; Peter, L. M.; Cameron, P. J. Characterization of Planar Lead Halide Perovskite Solar Cells by Impedance Spectroscopy, Open Circuit Photovoltage Decay and Intensity-Modulated Photovoltage/Photocurrent Spectroscopy. *J. Phys. Chem. C* **2015**, *119*, 3456–3465. 406
- (10) Sanchez, R. S.; Gonzalez-Pedro, V.; Lee, J.-W.; Park, N.-G.; Kang, Y. S.; Mora-Sero, I.; Bisquert, J. Slow Dynamic Processes in Lead Halide Perovskite Solar Cells. Characteristic Times and Hysteresis. *J. Phys. Chem. Lett.* **2014**, *5*, 2357–2363. 407
- (11) Xiao, Z.; Yuan, Y.; Shao, Y.; Wang, Q.; Dong, Q.; Bi, C.; Sharma, P.; Gruverman, A.; Huang, J. Giant Switchable Photovoltaic Effect in Organometal Trihalide Perovskite Devices. *Nat. Mater.* **2015**, *14*, 193–198. 408
- (12) Juarez-Perez, E. J.; Sanchez, R. S.; Badia, L.; Garcia-Belmonte, G.; Kang, Y. S.; Mora-Sero, I.; Bisquert, J. Photoinduced Giant Dielectric Constant in Lead Halide Perovskite Solar Cells. *J. Phys. Chem. Lett.* **2014**, *5*, 2390–2394. 409
- (13) Wu, X.; Yu, H.; Li, L.; Wang, F.; Xu, H.; Zhao, N. Composition-Dependent Light-Induced Dipole Moment Change in Organometal Halide Perovskites. *J. Phys. Chem. C* **2014**, *119*, 1253–1259. 410

- 449 (14) Kim, M.; Im, J.; Freeman, A. J.; Ihm, J.; Jin, H. Switchable $S = 1/$
450 2 and $J = 1/2$ Rashba Bands in Ferroelectric Halide Perovskites. *Proc.*
451 *Natl. Acad. Sci. U.S.A.* **2014**, *111*, 6900–6904.
- 452 (15) Poglitsch, A.; Weber, D. Dynamic Disorder in Methylammo-
453 niumtrihalogenoplumbates (II) Observed by Millimeter Wave Spec-
454 troscopy. *J. Chem. Phys.* **1987**, *87*, 6373–6378.
- 455 (16) Frost, J. M.; Butler, K. T.; Brivio, F.; Hendon, C. H.; van
456 Schilfgaarde, M.; Walsh, A. Atomistic Origins of High-Performance in
457 Hybrid Halide Perovskite Solar Cells. *Nano Lett.* **2014**, *14*, 2584–
458 2590.
- 459 (17) Frost, J. M.; Butler, K. T.; Walsh, A. Molecular Ferroelectric
460 Contributions to Anomalous Hysteresis in Hybrid Perovskite Solar
461 Cells. *APL Mater.* **2014**, *2*, 081506.
- 462 (18) Liu, S.; Zheng, F.; Koocher, N. Z.; Takenaka, H.; Wang, F.;
463 Rappe, A. M. Ferroelectric Domain Wall Induced Band-Gap
464 Reduction and Charge Separation in Organometal Halide Perovskites.
465 *J. Phys. Chem. Lett.* **2015**, *6*, 693–699.
- 466 (19) Kawamura, Y.; Mashiyama, H.; Hasebe, K. Structural Study on
467 Cubic-Tetragonal Transition of $\text{CH}_3\text{NH}_3\text{PbI}_3$. *J. Phys. Soc. Jpn.* **2002**,
468 *71*, 1694–1697.
- 469 (20) Mashiyama, H.; Magome, E.; Kawamura, Y.; Kubota, Y.
470 Displacive Character of the Cubic-Tetragonal Transition in
471 $\text{CH}_3\text{NH}_3\text{PbX}_3$. *J. Korean Phys. Soc.* **2003**, *42*, 1026–1029.
- 472 (21) Wei, J.; Zhao, Y.; Li, H.; Li, G.; Pan, J.; Xu, D.; Zhao, Q.; Yu, D.
473 Hysteresis Analysis Based on the Ferroelectric Effect in Hybrid
474 Perovskite Solar Cells. *J. Phys. Chem. Lett.* **2014**, 3937–3945.
- 475 (22) Chen, H.-W.; Sakai, N.; Ikegami, M.; Miyasaka, T. Emergence of
476 Hysteresis and Transient Ferroelectric Response in Organo-Lead
477 Halide Perovskite Solar Cells. *J. Phys. Chem. Lett.* **2014**, *6*, 164–169.
- 478 (23) Kutes, Y.; Ye, L. H.; Zhou, Y. Y.; Pang, S. P.; Huey, B. D.;
479 Padture, N. P. Direct Observation of Ferroelectric Domains in
480 Solution-Processed $\text{CH}_3\text{NH}_3\text{PbI}_3$ Perovskite Thin Films. *J. Phys.*
481 *Chem. Lett.* **2014**, *5*, 3335–3339.
- 482 (24) Balke, N.; Maksymovych, P.; Jesse, S.; Kravchenko, I.; Li, Q.;
483 Kalinin, S. Exploring Local Electrostatic Effects with Scanning Probe
484 Microscopy: Implications for Piezoresponse Force Microscopy and
485 Triboelectricity. *ACS Nano* **2014**, *8*, 10229–10236.
- 486 (25) Kalinin, S.; Kumar, A.; Balke, N.; McCorkle, M.; Guo, S. L.;
487 Arruda, T.; Jesse, S. ESM of Ionic and Electrochemical Phenomena on
488 the Nanoscale. *Adv. Mater. Process* **2011**, *169*, 30–34.
- 489 (26) Kalinin, S. V.; Jesse, S.; Tselev, A.; Baddorf, A. P.; Balke, N. The
490 Role of Electrochemical Phenomena in Scanning Probe Microscopy of
491 Ferroelectric Thin Films. *ACS Nano* **2011**, *5*, 5683–5691.
- 492 (27) Im, J.-H.; Jang, I.-H.; Pellet, N.; Grätzel, M.; Park, N.-G. Growth
493 of $\text{CH}_3\text{NH}_3\text{PbI}_3$ Cuboids with Controlled Size for High-Efficiency
494 Perovskite Solar Cells. *Nat. Nano.* **2014**, *9*, 927–932.
- 495 (28) Dahan, D.; Molotskii, M.; Rosenman, G.; Rosenwaks, Y.
496 Ferroelectric Domain Inversion: The Role of Humidity. *Appl. Phys.*
497 *Lett.* **2006**, *89*, 152902.
- 498 (29) Lines, M. E.; Glass, A. M. *Principles and Applications of*
499 *Ferroelectrics and Related Materials*; Clarendon Press: Oxford, 2001.
- 500 (30) Bea, H.; Ziegler, B.; Bibes, M.; Barthelemy, A.; Paruch, P.
501 Nanoscale Polarization Switching Mechanisms in Multiferroic BiFeO_3
502 Thin Films. *J. Phys.: Condens. Matter* **2011**, *23*, 142201.
- 503 (31) Kalinin, S. V.; Rodriguez, B. J.; Jesse, S.; Shin, J.; Baddorf, A. P.;
504 Gupta, P.; Jain, H.; Williams, D. B.; Gruverman, A. Vector
505 Piezoresponse Force Microscopy. *Microsc. Microanal.* **2006**, *12*, 206–
506 220.
- 507 (32) Lefki, K.; Dormans, G. J. M. Measurement of Piezoelectric
508 Coefficients of Ferroelectric Thin Films. *J. Appl. Phys.* **1994**, *76*, 1764–
509 1767.
- 510 (33) Kholkin, A. L.; Iakovlev, S. O.; Baptista, J. L. Direct Effect of
511 Illumination on Ferroelectric Properties of Lead Zirconate Titanate
512 Thin Films. *Appl. Phys. Lett.* **2001**, *79*, 2055–2057.
- 513 (34) Kholkin, A. L.; Setter, N. Photoinduced Poling of Lead Titanate
514 Zirconate Thin Films. *Appl. Phys. Lett.* **1997**, *71*, 2854–2856.
- 515 (35) Zheng, F.; Takenaka, H.; Wang, F.; Koocher, N. Z.; Rappe, A.
516 M. First-Principles Calculation of the Bulk Photovoltaic Effect in
 $\text{CH}_3\text{NH}_3\text{PbI}_3$ and $\text{CH}_3\text{NH}_3\text{PbI}_{3-x}\text{Cl}_x$. *J. Phys. Chem. Lett.* **2015**, *6*, 31–
37. 517
518
519
520
521
522
523
524
525
526
527
528
529
530
531
532
533
534
535
536